Draft version March 28, 2013
Preprint typeset using LaTeX style emulateapj v. 5/2/11

ROTATING ACCRETION FLOWS: FROM INFINITY TO THE BLACK HOLE

Jason Li[1], Jeremiah Ostriker[1], & Rashid Sunyaev[2,3,4]
[1]Department of Astrophysical Sciences, Peyton Hall, Princeton University, Princeton, NJ 08544, USA
[2] Institute for Advanced Study, Einstein Drive, Princeton, New Jersey 08540, USA
[3] Max Planck Institut für Astrophysik, Karl-Schwarzschild-Str. 1 85741, Garching, Germany
[4] Space Research Institute, Russian Academy of Sciences, Profsoyuznaya 84/32, 117997 Moscow, Russia

Draft version March 28, 2013

ABSTRACT

Accretion onto a supermassive black hole of a rotating inflow is a particularly difficult problem to study because of the wide range of length scales involved. There have been broadly utilized analytic and numerical treatments of the global properties of accretion flows, but detailed numerical simulations are required to address certain critical aspects. We use the ZEUS code to run hydrodynamical simulations of rotating, axisymmetric accretion flows with Bremsstrahlung cooling, considering solutions for which the centrifugal balance radius significantly exceeds the Schwarzschild radius, with and without viscous angular momentum transport. Infalling gas is followed from well beyond the Bondi radius down to the vicinity of the black hole. We produce a continuum of solutions with respect to the single parameter $\dot{M}_{\rm B}/\dot{M}_{\rm Edd}$, and there is a sharp transition between two general classes of solutions at an Eddington ratio of $\dot{M}_{\rm B}/\dot{M}_{\rm Edd} \sim {\rm few} \times 10^{-2}$. Our high inflow solutions are very similar to the standard Shakura & Sunyaev (1973) results. But our low inflow results are to zeroth order the stationary Papaloizou and Pringle (1984) solution, which has no accretion. To next order in the small, assumed viscosity they show circulation, with disk and conical wind outflows almost balancing inflow. These solutions are characterized by hot, vertically extended disks, and net accretion proceeds at an extremely low rate, only of order α times the inflow rate. Our simulations have converged with respect to spatial resolution and temporal duration, and they do not depend strongly on our choice of boundary conditions.

Subject headings: accretion: accretion disks - black hole physics - quasars: general - X-rays: general

1. INTRODUCTION

Supermassive Black Hole accretion is affected by the properties of the accretion flow on a wide range of length scales. Gravity and gas dynamics play an important role from the gravitational radius out to much larger distances where the gravitational potential energy of the gas is comparable to its kinetic energy. The properties of the infalling gas at even larger radii, where gravity is weak can also in principle affect the global properties of the accretion flow, an important point that is sometimes overlooked in studies of accretion physics.

In the unmagnetized spherically symmetric case with no angular momentum and adiabatic equation of state, the global accretion flow is given by the Bondi solution (Bondi 1952). The Bondi radius $R_{\rm B} \equiv GM_{\rm BH}/c_{s,\infty}^2$ sets the scale at which gravity becomes important, and the mass accretion rate is given by $\dot{M}_{\rm B} \equiv \Lambda 4\pi r_{\rm B}^2 \rho_\infty c_{s,\infty}$. $M_{\rm BH}$ here is the black hole mass, ρ_∞ is the mass density of gas at infinity, $c_{s,\infty}$ is the gas sound speed at infinity, and $\Lambda \equiv [2/(5-3\gamma)]^{(5-3\gamma)/[2(\gamma-1)]}/4$ (Frank et al. 2002), where γ is the adiabatic index. The introduction of angular momentum fundamentally modifies this picture, however, and for sufficiently high angular momentum the gas can no longer accrete onto the central black hole. For gas with specific angular momentum j, the centrifugal radius $R_{\rm c} \equiv j^2/GM_{\rm BH}$ defines the radius interior to which the gas has difficulty penetrating. Accretion in this case requires some form of angular momentum transport. Turbulent stresses associated with the nonlinear development of the MagnetoRotational Instability (MRI) are thought to be capable of transporting angular momentum (Velikhov 1959; Chandrasekhar 1960; Balbus & Hawley 1991). The angular momentum transport properties of the MRI are often parameterized with an effective shear viscosity $\nu \equiv \alpha c_s H_p$, where numerical simulations suggest α is typically of order 0.01 (Stone et al. 1996; Hawley et al. 2011; McKinney et al. 2012). Observations actually suggest a vertically and azimuthally averaged $\alpha \sim 0.1 - 0.4$ (King 2007), a discrepancy that to date has not yet been fully addressed.

There are a number of general classes of analytic solutions for rotating flows with viscous angular momentum transport. The standard solution in the limit of a geometrically thin and optically thick viscous disk was given by Shakura & Sunyaev (1973; see also Lynden-Bell & Pringle 1974, Novikov & Thorne 1973), commonly referred to as an α-disk. Thin disks typically neglect global heat transport and only consider effects that are first order in the disk thickness H/R, where H is the disk thickness at cylindrical radius R. The next order of approximation is slim disks, which account for terms in the equations of motion that are second order in the disk thickness H/R (Abramowicz et al. 1988; see also Abramowicz et al. 1986, Kato et al. 1988, Chen & Taam 1993, Narayan & Popham 1993, Katz 1977, Begelman 1978, Begelman & Meier 1982, Eggum et al. 1988). Slim disks allow for non-negligible ra-

jgli@astro.princeton.edu

dial velocity, horizontal pressure gradients, and advective heat transport, and they have been used to model geometrically thick, hot disks accreting at super-Eddington rates. Advection Dominated Accretion Flows (ADAFs, Narayan & Yi 1994, 1995a,b; Abramowicz et al. 1995; Ichimaru 1977; Rees et al. 1982; Quataert & Narayan 1999a; Narayan & Fabian 2011) describe radiatively inefficient sub-Eddington flows. The accreting low density gas is hot and geometrically extended in the polar direction, and the thermal energy is advected onto the central object. The closely related Adiabatic Inflow Outflow Solutions (ADIOS, Blandford & Begelman 1999; Begelman 2011) can accrete at much lower rates by allowing for outflows that can carry off energy and angular momentum (see also Jiao & Wu 2011). At present it is unclear which, if any, of these solutions real supermassive black hole accretion flows will pick. Certainly for hot disks with $H \sim R$, the standard approximations in thin disk accretion theory break down (Pringle 1981), and we should consider terms of all order in H/R. Further study of the detailed properties of geometrically thick disks is required.

Numerical simulations have provided further insight on accretion physics, and Convection Dominated Accretion Flows (CDAFs; Igumenshchev & Abramowicz 1999, 2000; Igumenshchev et al. 2000, 2003; Stone et al. 1999; Narayan et al. 2000; Quataert & Gruzinov 2000) , which operate in the weak viscosity regime for flows with no cooling, have been proposed to explain one class of simulations. Recent work by Yuan et al. (2012b) tends to favor ADIOS-type models over CDAFs, however. Other authors have studied the geometry of two dimensional magnetohydrodynamical flows accreting from torus-like initial reservoirs of gas (Stone & Pringle (2001); Hawley et al. (2001); Machida et al. (2001); Igumenshchev & Narayan (2002); Hawley & Balbus (2002); see also Narayan et al. (2012) for 3D simulations with general relativity). Many previous works neglect the radiative properties of the flow, however, which may play an important role in determining the geometry of the flow (Dibi et al. 2011; Fragile et al. 2012). For accretion flows with radiative cooling, the properties of the infalling gas at infinity determine the strength of the radiative cooling and can affect the global properties of the flow (Yuan et al. 2000). Several authors mimic cooling by varying the adiabatic index of the gas (Moscibrodzka & Proga 2008, 2009; Janiuk et al. 2009) or include radiative transfer (Ohsuga et al. 2009; Ohsuga & Mineshige 2011; see also Zanotti et al. 2011, and references therein), but accretion in these works is aided by at least some inflowing gas that has low angular momentum or starting with gas that is bound to the black hole. Another important consequence of radiation from gas near the black hole is that it can drastically transform the outer parts of the accretion flow via heating (Park & Ostriker 2001, 2007).

It is well known that observed black holes can accrete at rates that are only a small fraction of the Bondi accretion rate. For example, Sgr A* appears to be accreting at a rate of $10^{-3} - 10^{-2}\dot{M}_{\rm B}$ (Yuan et al. 2003; Quataert 2004). A number of authors have studied the transition between the cooling flow at large radii and the accretion flow near and below the Bondi radius (Quataert & Narayan 1999b; Quataert & Narayan 2000), and the implications for accretion rates. Various energy transport mechanisms have been suggested that may be able to reduce accretion rates well below the Bondi rate (Ciotti & Ostriker 2001; Quataert 2004; Sharma et al. 2008; Shcherbakov 2010; Igumenshchev 2006). Other authors have invoked Radiatively Inefficient Accretion Flows to explain the low luminosity of observed accreting systems (Narayan & McClintock 2008, and references therein). We consider here the alternate view that it is simply the angular momentum of the gas that slows accretion. There has been some analytic and semi-analytic work exploring this idea, including angular momentum transport (Xu & Chen 1997; Blandford & Begelman 1999), and both angular momentum transport and cooling (e.g., Chakrabarti 1996; Park 2009; Inogamov & Sunyaev 2010), as well as numerical work without cooling (e.g., Stone et al. 1999; Proga & Begelman 2003a,b; Yuan et al. 2012a,b) and with cooling (Yuan & Bu 2010).

This paper will treat the accretion problem in the domain where the angular momentum is not sufficient to prevent inflow at the Bondi rate but ample to inhibit accretion without the operation of some viscous process. That is, we will work exclusively in the domain

$$R_s \ll R_{\rm c} \ll R_{\rm B}, \tag{1}$$

where $R_s \equiv 2GM_{\rm BH}/c^2$ is the Schwarzschild radius. Since the ratio of the bounding radii, $R_{\rm B}/R_s \sim 10^8/T_4$, this choice is well-defined. Moreover, many elliptical galaxies, including M87, have stellar populations with small average spin that is insufficient to create Keplerian disks near the Bondi radius (see e.g., Inogamov & Sunyaev 2010). We run hydrodynamical simulations to follow infalling, radiating gas that starts from well beyond the Bondi radius with $Be > c_{s,\infty}^2/(\gamma - 1)$ (see Equation 10) down to the vicinity of the black hole. We include shear viscosity to capture qualitatively the angular momentum transport properties of the MRI, and so accretion can proceed at varying rates, depending on the flow parameters. Since the gravitational and centrifugal forces do not have the same scaling with radial distance in our setup, we do not expect our solutions to be self-similar as in standard ADAF (Narayan & Yi 1994) and CDAF models(Quataert & Gruzinov 2000; Narayan et al. 2000). The thermal Bremsstrahlung cooling can also play an essential role in the energetics of the flow and determine if gas is bound to the black hole or not. We provide accretion flow solutions in both the very sub-Eddington, nearly adiabatic domain, and also solutions approaching the super-Eddington domain. Section 2 provides the mathematical framework framework for our problem and describes our numerical method. Section 3 gives our main results, and the broader implications of our results are discussed in sections 4 and 5. The Appendix provides details on the convergence properties of our solutions. We will designate the low inflow solutions that we find as "RRIOS" - Radiating Rotating Inflow-Outflow Solutions.

2. METHOD

2.1. *Equations*

We use ZEUS-2D v2.0 (Stone & Norman 1992) to solve the equations of hydrodynamics,

$$\left(\frac{\partial}{\partial t}+\boldsymbol{v}\cdot\boldsymbol{\nabla}\right)\rho+\rho\boldsymbol{\nabla}\cdot\boldsymbol{v}=0, \quad (2)$$

$$\rho\left(\frac{\partial}{\partial t}+\boldsymbol{v}\cdot\boldsymbol{\nabla}\right)\boldsymbol{v}=-\boldsymbol{\nabla}p-\rho\boldsymbol{\nabla}\Phi, \quad (3)$$

$$\rho\left(\frac{\partial}{\partial t}+\boldsymbol{v}\cdot\boldsymbol{\nabla}\right)\frac{e}{\rho}=-p\boldsymbol{\nabla}\cdot\boldsymbol{v}, \quad (4)$$

where ρ is mass density, $\boldsymbol{v}$ is flow velocity, e is energy density, gas pressure $p\equiv(\gamma-1)e$, where γ is the adiabatic index, and the gravitational potential $\Phi\equiv -GM_{\rm BH}/r$. We run global hydrodynamical simulations of axisymmetric rotating accretion flows in spherical polar coordinates. The simulations include thermal Bremsstrahlung cooling, shear viscosity to capture drag due to turbulent stresses, and modified boundary conditions to allow for disk and wind outflows. The source terms for momentum and energy in the ZEUS hydrocode are modified by the addition of the terms within square brackets below:

$$\rho\left(\frac{\partial\boldsymbol{v}}{\partial t}\right)_{\rm sources}=-\boldsymbol{\nabla}p-\rho\boldsymbol{\nabla}\Phi-\nabla\cdot\boldsymbol{Q}+\left[\boldsymbol{\nabla}\cdot\boldsymbol{\sigma'}\right], \quad (5)$$

and

$$\left(\frac{\partial e}{\partial t}\right)_{\rm sources}=-p\boldsymbol{\nabla}\cdot\boldsymbol{v}-\boldsymbol{Q}\cdot\boldsymbol{\nabla}\boldsymbol{v}+\left[\boldsymbol{\sigma'}\cdot\boldsymbol{\nabla}\boldsymbol{v}-\dot{e}_{\rm Brem}\right], \quad (6)$$

in which $\boldsymbol{\sigma'}$ is the viscous shear tensor and $\boldsymbol{q}$ is the heat flux due to thermal conduction of electrons. ZEUS' standard tensor artificial viscosity $\boldsymbol{Q}$ is applied with shocks spread over ≈ 2 zones, and we use a Foward Time Centered Space differencing scheme for our modified source terms. We neglect the non-azimuthal components of the viscous shear tensor $\boldsymbol{\sigma'}$, as it is believed that the poloidal shear is subdominant to the azimuthal shear in the nonlinear regime of the MRI (see Stone et al. 1999). The azimuthal components of the viscous shear tensor are

$$\boldsymbol{\sigma'}_{r\phi}=\nu\rho r\frac{\partial}{\partial r}\left(\frac{v_\phi}{r}\right), \quad (7)$$

$$\boldsymbol{\sigma'}_{\theta\phi}=\frac{\nu\rho\sin\theta}{r}\frac{\partial}{\partial\theta}\left(\frac{v_\phi}{\sin\theta}\right), \quad (8)$$

where ν is the kinematic viscosity. The Bremsstrahlung cooling term (Svensson 1982, Ball et al. 2001)

$$\dot{e}_{\rm Brem}\equiv\alpha_f r_e^2 m_e c^3 n^2 (32/3)(2/\pi)^{1/2}\left(\frac{k_B T}{m_e c^2}\right)^{1/2}, \quad (9)$$

where α_f is the fine structure constant and r_e is the classical electron radius. We use this abbreviated form for the Bremsstrahlung cooling to capture the qualitative effects of thermal emission; in fact in high temperature regions the electron component approaches relativistic speeds and Bremsstrahlung radiation increases substantially above equation (9). The cooling is limited by a floor in the temperature, equal to the gas temperature at the outer boundary, in order to maintain stability. The advective transport terms in ZEUS are unmodified.

2.2. *Setup & Flow Properties*

In our simulations gas flows in through the outer boundary, located at $R_{\rm out}=10R_B$, at the Bondi rate, $\dot{M}_{\rm B}$. We modify the outer boundary condition locally to an outflow boundary condition in whichever grid zones at the outer boundary that the flow is moving radially outward, however. We note that several other authors have studied accretion flows with outer boundary near the Bondi radius (e.g., Pen et al. 2003; Pang et al. 2011). Our inner boundary, located at $R_{\rm in}=10^{-3}R_B$, is a standard no torque outflow boundary condition. $R_{\rm in}$ is located at $91R_s$, and we have checked the convergence of our results with respect to the location of the inner boundary (see Appendix). The flow is initialized throughout with Bondi profile for density, energy density, and radial velocity. Our standard simulations are run with $T_\infty=2\times10^7$ K. This is close to the temperature of gas heated radiatively by a typical quasar output spectrum (Sazonov et al. 2005). The simulations are run with adiabatic index $\gamma=1.5$, except where otherwise noted, and we verify explicitly that this assumption does not affect our main results (cf Figure 7). The real gas will have $\gamma=5/3$ above $R\sim300-500R_s$. At lower radii, in the non-collisional case, electrons become relativistic while protons are nonrelativistic, leading to lower effective γ. Our choice for γ is made in order to allow us to well separate the sonic and centrifugal radii for supersonic infall. The density at infinity, ρ_∞, is a parameter that determines the dimensionless quantity $\dot{M}_{\rm B}/\dot{M}_{\rm Edd}$, where $\dot{M}_{\rm Edd}\equiv 4\pi GM_{\rm BH}m_p/\epsilon\sigma_T c$ is the Eddington luminosity and we assume an efficiency $\epsilon=0.1$. This dimensionless mass accretion rate parameter scales as $\dot{M}_{\rm B}/\dot{M}_{\rm Edd}\propto M_{\rm BH}\rho_\infty/c_{s,\infty}^3$. The dimensionless cooling fraction $\dot{e}_{\rm Brem}\Delta t_{\rm char}/nkT\propto M_{\rm BH}\rho_\infty/c_{s,\infty}^4$, where we have taken characteristic time $\Delta t_{\rm char}=M_{\rm BH}/c_{s,\infty}^4$. The black hole mass and gas density at infinity appear together in the above two quantities, and the free parameter in the accretion flow is actually the product $M_{\rm BH}\rho_\infty$ (see Chang & Ostriker 1985). This parameter effectively determines the strength of the Bremsstrahlung cooling, with $\dot{M}_{\rm B}/\dot{M}_{\rm Edd}\ll1$ corresponding to no cooling and $\dot{M}_{\rm B}/\dot{M}_{\rm Edd}\gg1$ corresponding to strong cooling. For convenience we pick $M_{\rm BH}=2\times10^8M_\odot$ and allow ρ_∞ to vary freely. At $\rho_\infty=2.3\times10^{-21}g\,cm^{-3}$, the Eddington ratio $\dot{M}_{\rm B}/\dot{M}_{\rm Edd}=0.1$.

Gas is initialized with constant specific angular momentum throughout, except near the rotation axis, where it tapers to zero. The inflowing gas at the outer boundary has the same angular momentum, without tapering, ensuring that after initial transients, the gas has uniform angular momentum throughout. For adiabatic inviscid flows, the Bernoulli constant

$$Be\equiv\frac{1}{2}\left(v_r^2+v_\theta^2\right)+\frac{1}{2}\frac{j^2}{\varpi^2}-\frac{GM}{r}+\frac{c_s^2}{\gamma-1}, \quad (10)$$

where ϖ is cylindrical radius, is a conserved quantity (see e.g., Narayan & Yi 1994). It immediately follows that there is a centrifugal radius interior to which the gas cannot penetrate if gas starts from rest at infinity with $Be=\gamma c_{s,\infty}^2/(\gamma-1)$. The specific angular momentum is another free parameter in our simulations, but

we pick $j_\infty = \sqrt{0.02} R_{\rm B} c_{s,\infty}$ so that the centrifugal radius $R_{\rm c} = 0.02 R_{\rm B}$ is well resolved and lies at a radius 20 times that of the inner boundary. Hence we are computing within the domain given by equation (1). The limit of weak angular momentum with $R_{\rm c} \ll R_{\rm in}$ approaches the Bondi solution. For our choice of specific angular momentum, the introduction of shear viscosity and angular momentum transport allows for gas to migrate from the centrifugal radius down to the inner boundary and to accrete. The accreting gas carries only a small fraction ($< 20\%$) of the initial angular momentum j_∞ through the inner boundary. In our simulations we set the kinematic viscosity ν to a constant nonzero value $\nu = 10^{-3} c_{s,\infty} R_{\rm B}$. The effective α coefficient, $\alpha \equiv \nu / c_s H_p$, where c_s is the local sound speed and H_p the local pressure scale height (see Section 3.3), is then spatially variable, but is typically of order ~ 0.01 near the centrifugal barrier where the density peaks. Stone et al. (1999) found that the properties of their non-radiative hydrodynamic flow do not depend strongly on the assumed form for kinematic viscosity, and Stone & Pringle (2001) found weakly magnetized flows to be qualitatively similar to the viscous hydrodynamic ones. Incidentally, the limit of large specific angular momentum with $R_{\rm c} \gtrsim R_{\rm B}$ should approach that of a giant viscous disk with large radial extent, but we have not explored this regime in any detail. The Bremsstrahlung cooling also modifies the flow profile, and for cold disks the inflow can be highly supersonic. In these cold solutions the sonic radius is typically intermediate between but still well separated from the centrifugal and Bondi radii.

2.3. *Numerics*

Our standard simulations are run with 21 equally spaced grid zones in polar angle θ varying from $\theta = 0$ to $\theta = \pi/2$, enforcing symmetry across the equatorial plane. In the radial direction we use a non-uniform logarithmic grid with 32 zones per decade ranging from $R_{\rm in} = 10^{-3} R_{\rm B}$ to $R_{\rm out} = 10 R_{\rm B}$, with 128 total grid zones. As a code check, we ran the spherically symmetric test problem with no cooling. Our code is able to maintain the Bondi profile for mass density and radial velocity to within 5% for various values of the adiabatic index γ. The internal energy density is less well conserved in the very inner portions of the flow (≈ 10 innermost cells) due to artificial viscous heating, but is still within a factor of ≈ 2 of the Bondi solution. The simulations are run until all time-averaged gross quantifiers of the flow structure approach quasi-steady values. All diagnostics of the flow are averaged over many tens of Bondi times $t_{\rm B} \equiv R_{\rm B}/c_{s,\infty}$, typically between times $t = 40\, t_{\rm B}$ and $t = 90\, t_{\rm B}$ (see Appendix). Flow patterns are illustrated at time $t = 90\, t_{\rm B}$ except where otherwise noted. The code is mass conservative, so mass flowing inwards from large radii must accumulate on the grid or outflow either through the inner boundary or back out to large radii via the combination of polar and equatorial outflow.

We also run a number of tests to check the proper implementation of the additional physics we have added to ZEUS. We verified the proper thermal cooling of a stationary constant density gas, as well as the diffusion of thermal energy when a temperature gradient exists. Finally, we have reproduced qualitatively the viscous evolution of an initial ring of matter (Pringle 1981). The ring spreads in radius as matter moves inwards, but the bulk of the angular momentum is transferred outwards. Kinetic energy lost to viscous dissipation is added to the internal energy of the gas, with the viscous substep of the code conserving energy to within 10%.

3. RESULTS

3.1. *Adiabatic Inviscid Flows*

For adiabatic flows with sufficiently high angular momentum that the centrifugal barrier is located far from the black hole, equation (10) immediately tells us that there can be no accretion onto the black hole. Any inflowing high angular momentum material must either accumulate beyond the centrifugal radius or be deflected back outwards and ejected in outflows (Proga & Begelman see 2003a, and references therein; see also Hawley et al. 1984a,b; Hawley & Smarr 1986).

In the adiabatic regime with constant angular momentum j throughout, there is a stationary ($v_r = v_\theta = 0$) settling solution satisfying the momentum equation (see Papaloizou & Pringle 1984; Fishbone & Moncrief 1976). Starting from the momentum equation,

$$-\frac{1}{\rho}\boldsymbol{\nabla} p - \boldsymbol{\nabla}\Phi + \frac{j^2}{\varpi^3}\hat{\boldsymbol{\varpi}} = 0, \tag{11}$$

the adiabatic relation $p \propto \rho^\gamma$ gives

$$\boldsymbol{\nabla}\left(\frac{c_s^2}{\gamma - 1} + \Phi + \frac{j^2}{2\varpi^2}\right) = 0. \tag{12}$$

This yields an equation for the sound speed,

$$\frac{c_s^2}{c_{s,\infty}^2} = 1 + (\gamma - 1)\frac{GM}{c_{s,\infty}^2 r} - \frac{\gamma - 1}{2}\frac{j^2}{c_{s,\infty}^2 \varpi^2}, \tag{13}$$

valid where the right hand side is positive, as well as the density profile,

$$\frac{\rho}{\rho_\infty} = \left[1 + (\gamma - 1)\frac{GM}{c_{s,\infty}^2 r} - \frac{\gamma - 1}{2}\frac{j^2}{c_{s,\infty}^2 \varpi^2}\right]^{1/(\gamma - 1)}. \tag{14}$$

The density is zero near the polar axis in the region where the right hand side of equation (13) is negative. This solution is actually dynamically unstable to non-axisymmetric perturbations (Papaloizou & Pringle 1984), which we do not allow for in our axisymmetric code. Neglecting these instabilities is likely a reasonable assumption, however, as we have angular momentum gradients that can stabilize the flow (Papaloizou & Pringle 1987).

Our multidimensional adiabatic simulations closely resemble this stationary settling solution, with sound speed profile matching equation (13) to within a few percent exterior to the centrifugal barrier. Figure 1a shows the structure of the flow within the Bondi radius at Eddington ratio $\dot{M}_{\rm B}/\dot{M}_{\rm Edd} = 10^{-4}$. The red contours are logarithmic contours of density, given in cgs units, and we overlay black contours of logarithmic density for the adiabatic settling solution. The solid black line shows the zero density surface in the stationary solution. Blue arrows indicate vectors of mass flux in the $R-z$ plane, with length proportional to the magnitude of the mass flux vector. Subsequent diagrams of flow patterns showing logarithmic density contours and mass flux vectors are

illustrated in a similar fashion. The pressure associated with the accumulation of matter in an extended torus impedes the inflow of matter, as in the stationary solution. Indeed, the mass inflow rate at the Bondi radius is reduced by more than one order of magnitude to $\sim 0.06\dot{M}_{\rm B}$ at $t = 45t_{\rm B}$. There is evidence of time-dependent circulation, however, partially due to our choice of initial conditions, and the flow is not purely stationary with zero inflow rate at the Bondi radius. Matter flows inwards at intermediate latitudes and turns around at radii exterior to the centrifugal barrier, flowing back outwards in the polar and equatorial regions. Figure 1b shows the flow structure interior to $0.1R_{\rm B}$, with centrifugal radius located at $R_{\rm c} = 0.02R_{\rm B}$. There is again evidence of time-dependent circulation, but the largest differences in the flow relative to the stationary solution occur near the polar axis where the stationary solution has zero mass density. There are very small inflows in the polar region due to angular momentum transport associated with numerical viscosity, but the accretion rate is extremely low, $\dot{M}_{\rm accretion} < 10^{-3}\dot{M}_{\rm B}$, i.e. any accretion is due to numerical error. In the absence of physical angular momentum transport the gas in the centrifugal barrier is stationary in the r and θ directions, cannot accrete, and its pressure prevents new gas from falling down to small radii. Our results indicate that in the limit of very long and accurate integrations the solution would approach the stationary solution given in equations (13) and (14), since there is no engine to drive circulation for adiabatic flows.

3.2. *Hot and Cold Disks*

We find two general states for rotating axisymmetric accretion flows with radiative cooling and viscous angular momentum transport: hot thick disks with low accretion having polar and disk outflows, and cold thin disks with high accretion and weak polar and disk outflows.

Figure 2a shows the flow structure interior to the Bondi radius for the hot disk with $\dot{M}_{\rm B}/\dot{M}_{\rm Edd} = 10^{-4}$. Red contours are logarithmic contours of density, blue vectors represent mass flux in the $R-z$ plane, and the solid black line indicates the zero density surface in the adiabatic settling solution. Gas flows inwards over a wide range of intermediate polar angles, and there are equatorial and polar outflows. The mass ejected in the polar outflow, $\sim 0.02\dot{M}_{\rm B}$, is similar in magnitude to the adiabatic case, and is again caused by inflowing matter turning around exterior to the centrifugal torus. The detailed properties of this circulation may depend on the length and accuracy of our numerical integrations. The equatorial outflow is driven primarily by azimuthal stresses associated with the shear viscosity, and it has magnitude $\sim 0.25\dot{M}_{\rm B}$ at the Bondi radius. The mass inflow rate through the Bondi radius increases over that in the inviscid case and essentially balances this equatorial outflow. Figure 2b shows red contours of specific angular momentum in units of $j_\infty = \sqrt{0.02}R_{\rm B}c_{s,\infty}$, with blue vectors indicating the flux of angular momentum. The purple contour shows where $j = j_\infty$; equatorward the gas has higher specific angular momentum, and poleward the gas has lower specific angular momentum. The equatorial outflow carries off the angular momentum of the gas that was accreted (Kolykhalov & Syunyaev 1979; Inogamov & Sunyaev 2010) and some of the angular momentum lost by the polar outflow.

Figure 3a shows logarithmic density contours and velocity vectors interior to $0.1R_{\rm B}$. The black line indicates the zero density surface in the stationary solution. Inflowing matter dumps angular momentum into the equatorial regions, and an outflow is driven beginning just beyond the centrifugal radius, located at $R_{\rm c} = 0.02R_{\rm B}$. The inflowing gas is able to penetrate below the centrifugal radius only due to the angular momentum transport, i.e. the assumed weak MRI induced viscosity. In Figure 3b, which shows logarithmic density contours and velocity vectors interior to half the centrifugal radius, we see that the gas accretes over a range of latitudes from a time-dependent, vertically extended, sub-Keplerian disk. The accretion rate is very low, however, with magnitude $\sim 4\times10^{-3}\dot{M}_{\rm B}$ of order α times the mass inflow rate. There is some accretion due to the angular momentum transport, but the bulk of the gas is too energetic, with $Be > c_{s,\infty}^2/(\gamma-1)$, and has too much angular momentum for much of it to accrete. This conclusion is in close agreement with that of Stone et al. (1999).

In the cold disk solutions, the non-adiabatic gas radiates energy and most of the gas cannot travel back out to infinity on energetic grounds since $Be < c_{s,\infty}^2/(\gamma-1)$. In the absence of angular momentum transport the gas continuously accumulates near the centrifugal barrier. Gas pressure is insufficient to drive matter inward onto the central black hole and there is no steady solution. The introduction of angular momentum transport allows for significant accretion from the centrifugal torus, however. Figure 4a shows logarithmic density contours and mass flux vectors for the cold disk solution at Eddington ratio $\dot{M}_{\rm B}/\dot{M}_{\rm Edd} = 0.1$, interior to the Bondi radius. The solid black line shows the zero density surface in the adiabatic settling solution given in equation (14). Matter accumulates in an extended torus whose pressure slows mass inflow, similar in spirit to the adiabatic settling solution. Inflow proceeds at low polar angles $\theta \lesssim \pi/4$, however, with total inflow rate $\sim 0.45\dot{M}_{\rm B}$ at the Bondi radius. Equatorial gas exterior to the centrifugal barrier is still driven outwards by the viscous engine, but the outward propagation of the equatorial outflow is slowed by the strong radiative cooling. In the absence of external pressure, the equatorial outflow would continue to propagate outwards indefinitely (Kolykhalov & Syunyaev 1980). Our constant pressure outer boundary condition slows the outflow, however, and we find that the equatorial outflow is unable to propagate to the Bondi radius on time scales of order $\sim 100\,t_{\rm B}$. This solution is not technically a steady-state solution, as angular momentum is continuously dumped into the radially extended torus, which acts as a large sink of angular momentum. If we integrated for much longer times, however, the equatorial outflow must continue to propagate outwards to conserve momentum in a steady-state. Figure 4b shows logarithmic density contours and mass fluxes interior to $0.1R_{\rm B}$. The flow forms a geometrically thin disk, and angular momentum transport allows matter to continue to flow inwards from this disk. We illustrate the cold thin disk near the centrifugal barrier in greater detail in Figure 5. Red contours are again logarithmic density contours and blue vectors represent mass flux. Accretion proceeds through the inner boundary from the cold, thin, sub-

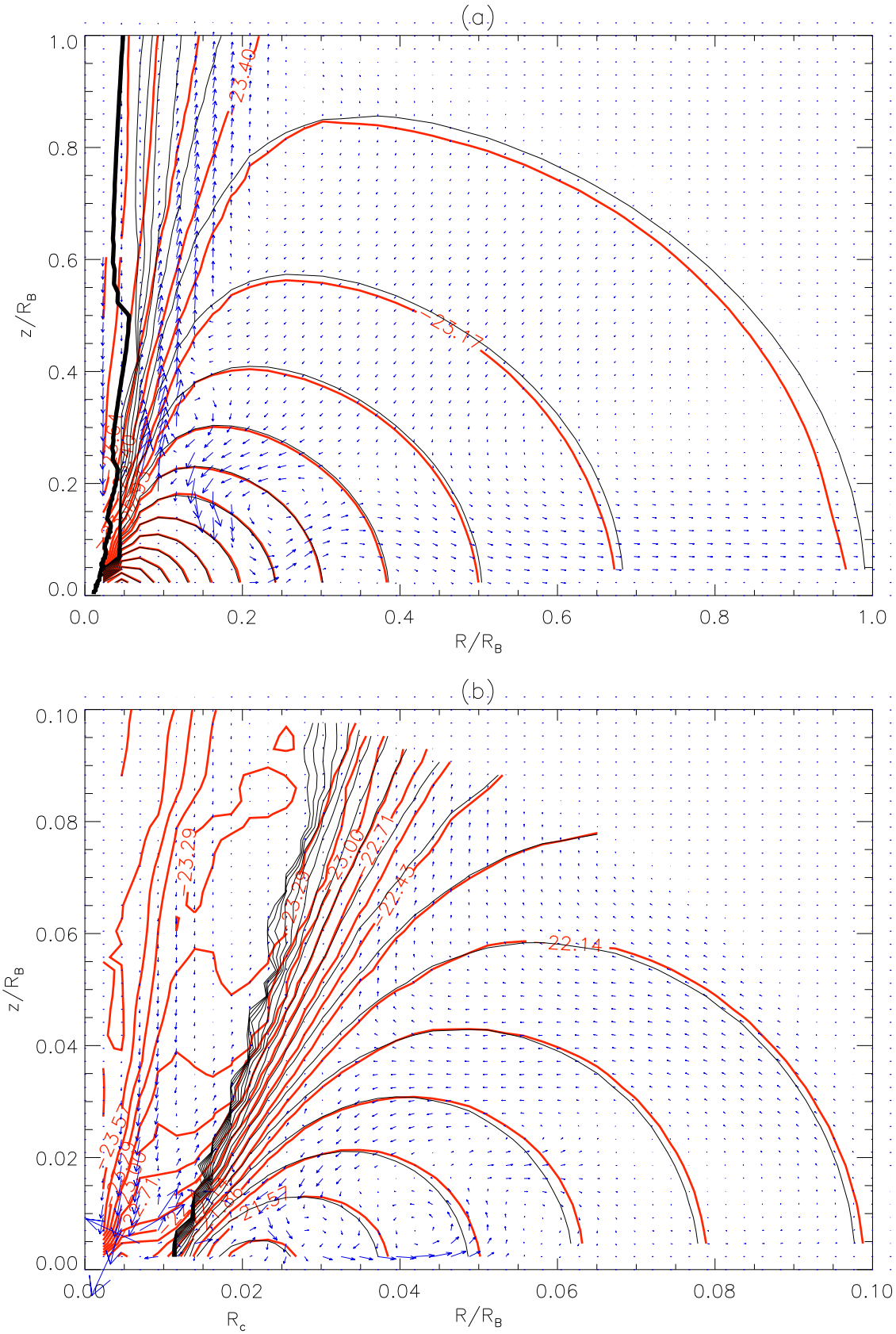

FIG. 1.— (a) The structure of the inviscid flow with no cooling, interior to $R_{\rm B}$ at $t = 45t_{\rm B}$. Red contours are logarithmic contours of density, and blue arrows indicate mass flux in the $R - z$ plane. The flow approaches a stationary settling solution (black contours, cf equation (14)) in which the inflow rate through the Bondi radius is reduced by an order of magnitude below the Bondi rate. The solid black line shows the zero density surface in the stationary solution. (b) Flow structure interior to $5R_{\rm c} = 0.1R_{\rm B}$. The bulk of the gas in the disk cannot accrete and the accretion through the polar funnel is negligible and due to numerical error.

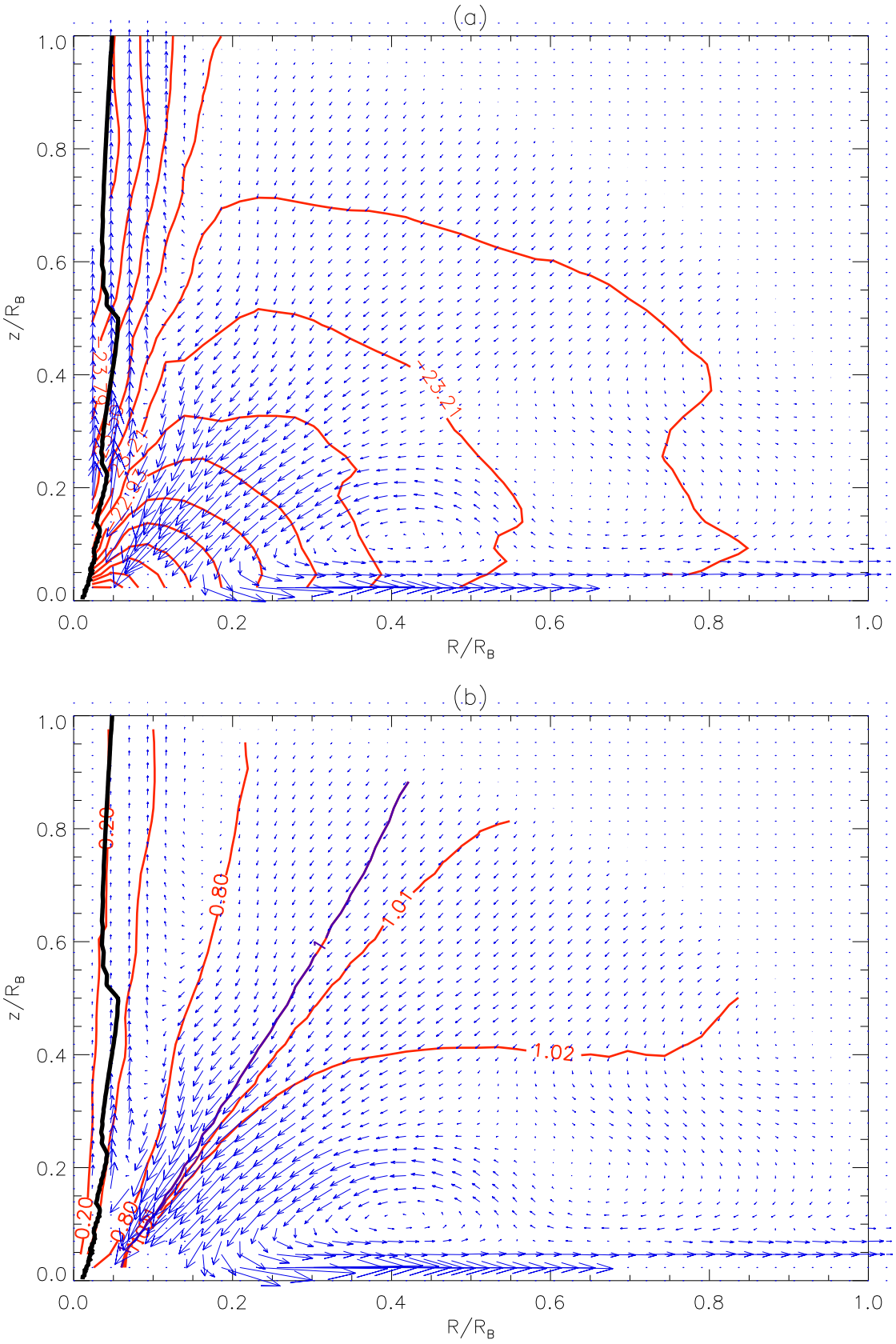

FIG. 2.— (a) The structure of the hot disk with angular momentum transport designed to mimic the MRI, shown interior to $R_{\rm B}$ in the low accretion limit where $\dot{M}_{\rm B}/\dot{M}_{\rm Edd} = 10^{-4}$. Cooling is negligible. Red contours are logarithmic contours of density, blue arrows indicate mass flux in the $R-z$ plane, and the black line demarcates the zero density surface in the adiabatic settling solution. Matter flows in through the Bondi radius and back out in disk and conical polar outflows. (b) Contours of specific angular momentum in units of $j_\infty = \sqrt{0.02} R_{\rm B} c_{s,\infty}$ and blue vectors of angular momentum flux. The black line demarcates the zero density surface in the stationary solution, and the purple contour marks where the specific angular momentum $j = j_\infty$. Angular momentum of inflowing material is transferred to the equatorial outflow.

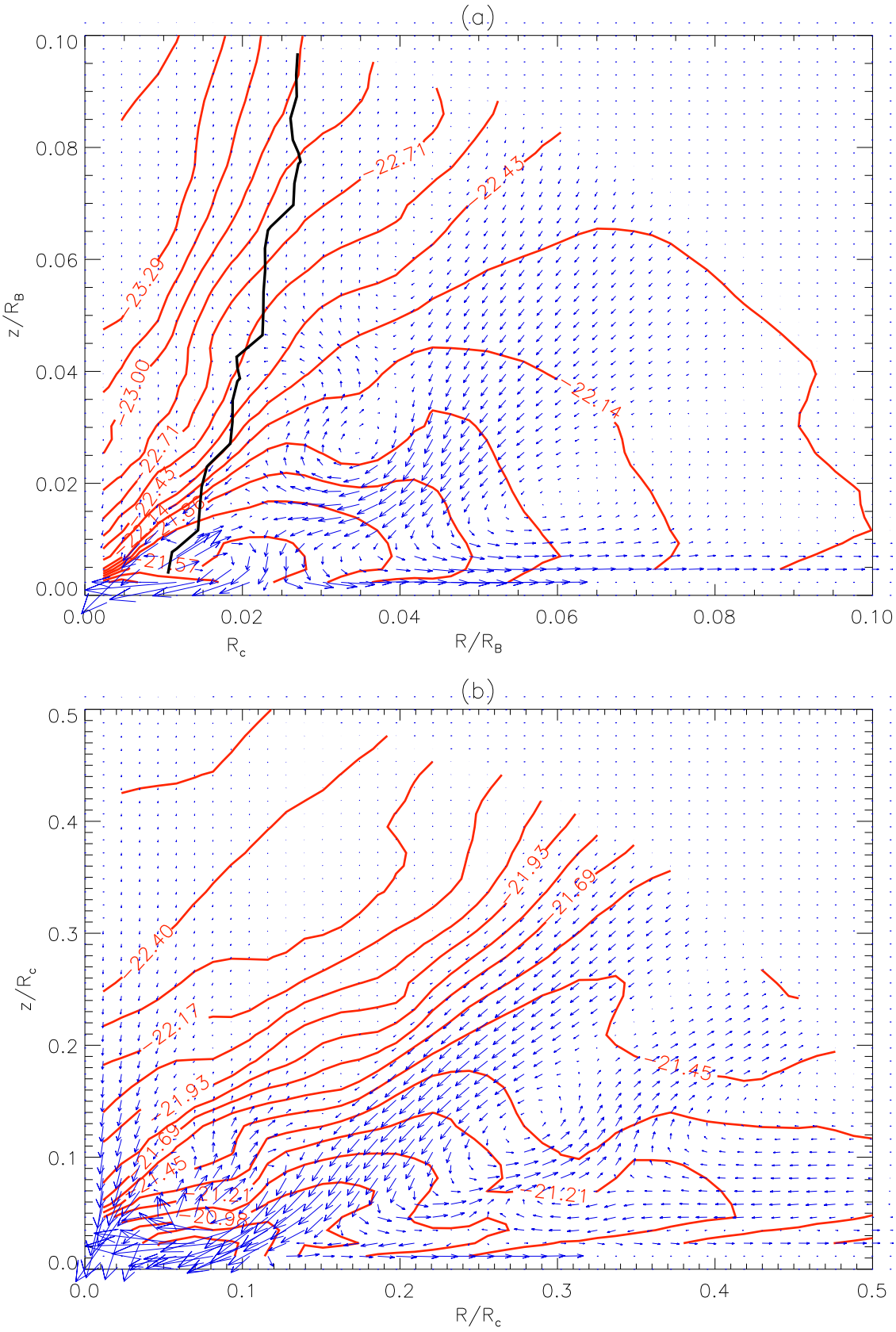

FIG. 3.— Closeup of the structure of the hot disk with angular momentum transport at Eddington ratio $\dot{M}_{\rm B}/\dot{M}_{\rm Edd} = 10^{-4}$. This is the same model as Figure 2. Red contours are logarithmic contours of density, and blue arrows represent mass flux in the $R-z$ plane. (a) Flow structure interior to $5R_{\rm c} = 0.1R_{\rm B}$. The black line shows the zero density surface in the adiabatic settling solution. Angular momentum transport allows a small amount of matter to inflow below the centrifugal radius, and viscous stresses drive a strong equatorial outflow. (b) Flow structure interior to half the centrifugal radius or $0.01R_{\rm B}$. Accretion proceeds at very low rates over a range of polar angles.

Keplerian disk, at a rate nearly equal to the mass inflow rate through the Bondi radius. This case resembles the standard thin disk (Shakura & Sunyaev 1973).

3.3. *Radiative Cooling*

Figure 6 shows the quasi-steady mass accretion rate through the inner boundary, the equatorial and polar wind mass outflow rates through the Bondi radius, and the mass inflow rate through the Bondi radius, all as functions of the parameter $\dot{M}_{\rm B}/\dot{M}_{\rm Edd}$. Crosses on the accretion rate curve indicate the Eddington ratios for which our simulations have converged with respect to temporal duration. For $\dot{M}_{\rm B}/\dot{M}_{\rm Edd} \lesssim 0.01$, the Bremsstrahlung cooling is weak and plays little dynamic role in the flow. The flow converges to a low accretion rate solution for $\dot{M}_{\rm B}/\dot{M}_{\rm Edd} \lesssim 10^{-3}$. The non-zero viscosity allows only a small fraction, $\sim 0.4\%$, of the inflowing matter at the Bondi radius to accrete onto the central black hole. The mass inflow rate at the Bondi radius $\dot{M}_{\rm inflow}$ is itself only $\sim 0.29\dot{M}_{\rm B}$ because the centrifugal torus and outflows significantly impede the inflow (cf Figures 2 and 3). The gas density on the equator is much larger than in the polar region, and the equatorial outflow dominates the outward mass and momentum flux at the Bondi radius. The equatorial outflow nearly matches the mass inflow rate at the Bondi radius, whereas the polar outflow is much less significant and an order of magnitude weaker than either. It is important to note, however, that viscous heating near the centrifugal radius leads to a buildup of thermal energy and can lead to intermittent episodes of convective overturning. The overturning episodes can last for $\sim 10t_B$, with outward mass fluxes over a broad range of polar angles and a significant fraction of the characteristic mass inflow rates. The filled boxes in Figure 6 represent estimates of the time-averaged polar mass outflows including these overturning episodes, which by definition are not included in our quasi-steady average mass fluxes (see Appendix for more detail).

The strength of the radiative cooling increases with the parameter $\dot{M}_{\rm B}/\dot{M}_{\rm Edd}$, and in the range $\dot{M}_{\rm B}/\dot{M}_{\rm Edd} \sim 0.01 - 0.1$ there is an abrupt transition in the properties of the flow to the strong cooling regime. For $\dot{M}_{\rm B}/\dot{M}_{\rm Edd} \sim 0.1$ the inflowing gas is impeded in the equatorial regions by gas pressure in an extended centrifugal torus (cf Figure 4), and matter flows in through the Bondi radius at roughly half the Bondi rate. Nearly the entirety of this inflowing gas is accreted onto the central black hole and the solutions approach the standard Shakura & Sunyaev (1973) picture. Most of the inflowing gas does not have enough energy to travel back out to infinity, and only a very small portion bounces off the centrifugal barrier and is ejected in a polar wind. The persistence of the polar wind is uncertain, and much higher resolution studies with additional physics such as magnetic fields and radiation are necessary to study the detailed properties of polar outflows. We emphasize again that the high Eddington ratio solutions are only quasi-steady (see Section 3.2), and the equatorial outflows would be stronger if we integrated for times $\gtrsim 1000R_{\rm B}/c_{s,\infty}$.

We have further verified that the low accretion rate solutions depend weakly on our choice of adiabatic index. Figure 7 shows the mass inflow rate from large radii, equatorial and polar outflow rates at $R_{\rm B}$, and accretion rate as a function of γ. Mass fluxes depend weakly on γ in the range $1.4 - 1.65$, and our ansatz $\gamma = 1.5$ should not significantly affect our results.

The high accretion rate flows from Figure 6 with $\dot{M}_{\rm B}/\dot{M}_{\rm Edd} > 0.1$ are cold and form a geometrically thin disk, and the low accretion rate flows with $\dot{M}_{\rm B}/\dot{M}_{\rm Edd} < 0.01$ are hot and form vertically extended disks. Figure 8a shows the emission weighted temperature,

$$< T > \equiv \frac{\int \dot{e}_{\rm Brem} T dV}{\int \dot{e}_{\rm Brem} dV}, \tag{15}$$

as a function of $\dot{M}_{\rm B}/\dot{M}_{\rm Edd}$. We show three characteristic temperature curves, from top to bottom averaged over the region interior to the centrifugal barrier, the total region within $0.1R_{\rm B}$, and in the centrifugal torus. The centrifugal torus is extremely dense and cools to a lower temperature (the floor that we set) than other parts of the flow at high Eddington ratios. The gas interior to the centrifugal barrier is hottest because the gas has penetrated deeper into the gravitational potential well. For low $\dot{M}_{\rm B}/\dot{M}_{\rm Edd} < 0.01$ the gas in the inner parts of the flow is hot and a sizable fraction of the centrifugal temperature

$$T_{\rm c} \equiv \frac{\mu m_p}{k_b \gamma} \frac{2GM_{\rm BH}}{R_{\rm c}} = 100 T_\infty, \tag{16}$$

where $\mu = 0.5$ is the mean molecular weight. Electrons become weakly relativistic at such temperatures, but we neglect in our computations the increase of the Bremsstrahlung energy losses for relativistic electrons. We measure the pressure scale height of the disk as the vertical distance at the centrifugal radius over which the pressure drops by a factor of e. The pressure scale height of the disk for the hot solutions with vertically extended disks is $H_p/R_{\rm c} \sim 0.75$ (see Figure 8b), and they have $\alpha \sim 0.01$ at the centrifugal barrier. The high accretion rate solutions with cold thin disks have pressure scale at the centrifugal radius $H_p/R_{\rm c} \sim 0.15$, covering ~ 5 cells in the highest resolution simulation (see Appendix). For a cold thin disk in hydrostatic equilibrium and with angular momentum $j = \sqrt{0.02} R_{\rm B} c_{s,\infty}$ we expect $H_p/R_{\rm c} = c_s/v_\phi = 0.07$. Since we fix the kinematic viscosity ν in our code, our cold disks have $\alpha \sim 0.4$ rather than $\alpha \sim 0.01$ at the centrifugal barrier. The code has difficulty running the cold solutions at lower viscosity, as there is significantly greater mass deposited near the centrifugal radius before accretion can proceed. The gas has cooled strongly and energetically cannot reach infinity, however, and we expect it to accrete independently of the strength of the viscosity, as long as it is non-zero. In any case, radiative transfer becomes important at Eddington ratios of $\sim$ few $\times 0.01$, physics that we do not include here. The precise location of the transition between thin and thick disks, as well as the density, luminosity, and optical depth of the thin disks, will depend on these choices.

The conical polar outflows, driven by inflowing matter bouncing off the centrifugal barrier, are in general weak, but they exist over a wide range of Eddington ratios. Figure 8c gives the half-opening angle of the polar outflow at the Bondi radius as a function of $\dot{M}_{\rm B}/\dot{M}_{\rm Edd}$.

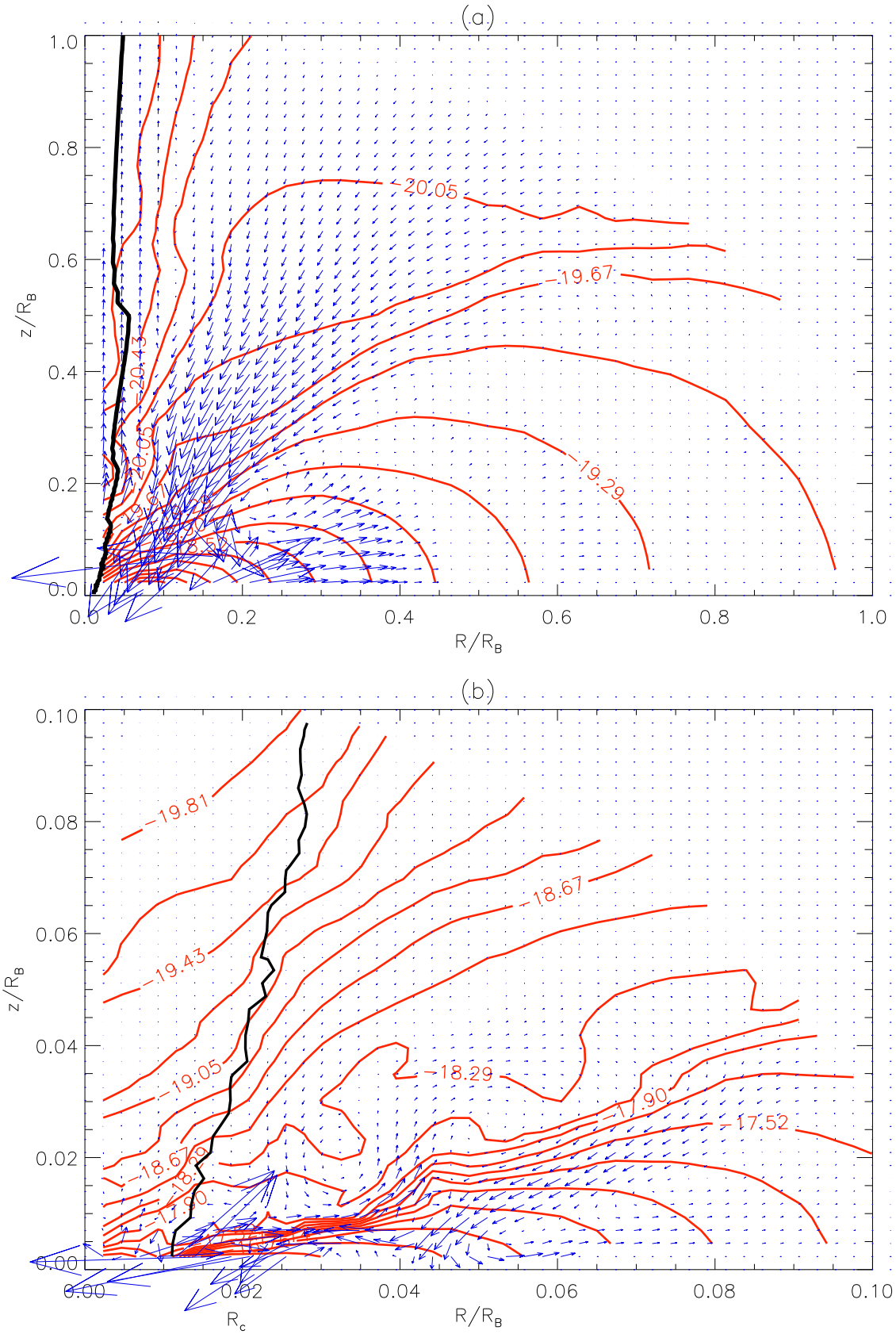

FIG. 4.— (a) The structure of the cold disk with angular momentum transport interior to $R_{\rm B}$, at Eddington ratio $\dot{M}_{\rm B}/\dot{M}_{\rm Edd} = 0.1$. Red contours are logarithmic contours of density, and blue arrows indicate mass flux in the $R - z$ plane. Inflow is impeded by gas pressure at large polar angles but proceeds through the Bondi radius at polar angles $\theta \lesssim \pi/4$. Angular momentum is dumped into the extended torus. (b) Flow structure interior to $5R_{\rm c} = 0.1R_{\rm B}$. Matter continues to flow inwards from a geometrically thin disk. This is the case which most closely approximates the standard Shakura-Sunyaev disk.

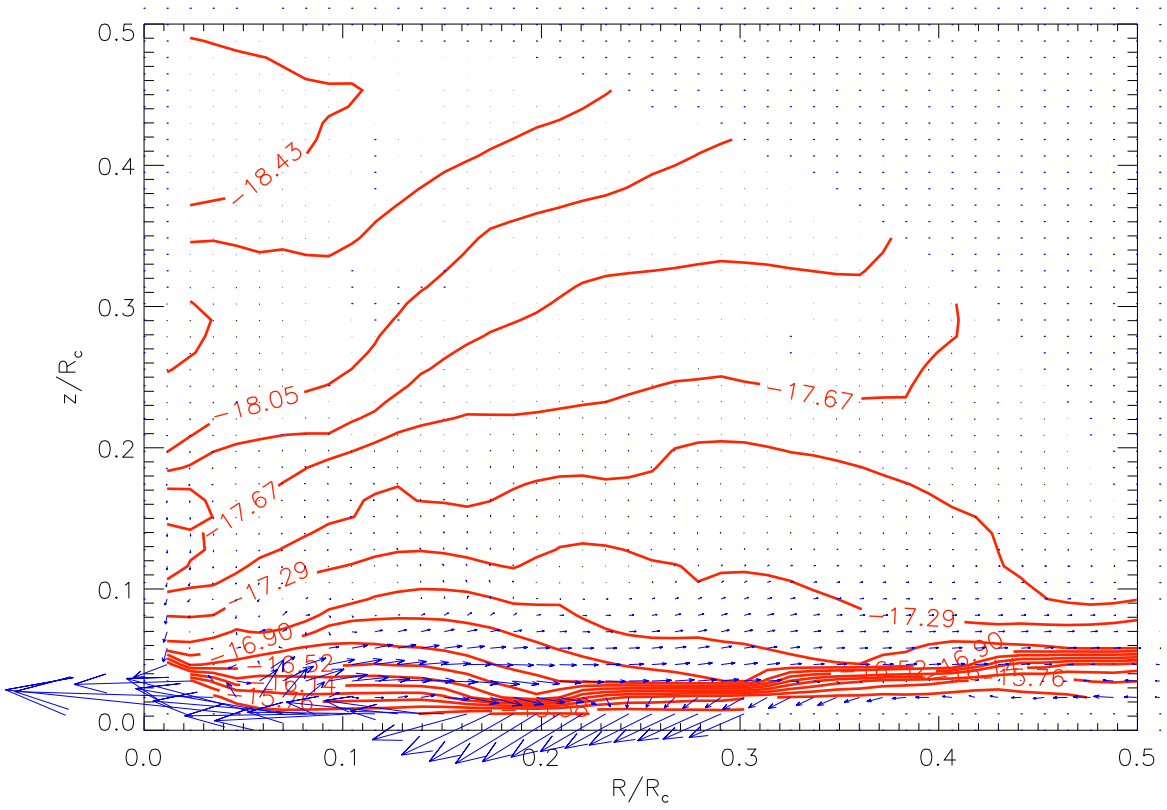

FIG. 5.— A closeup view of the high inflow case with $\dot{M}_{\rm B}/\dot{M}_{\rm Edd} = 0.1$. We show logarithmic density contours and mass flux vectors for the cold disk with angular momentum transport, interior to half the centrifugal radius. Matter accretes from the thin disk as in the standard Shakura & Sunyaev (1973) picture with angular momentum transport due to the MRI.

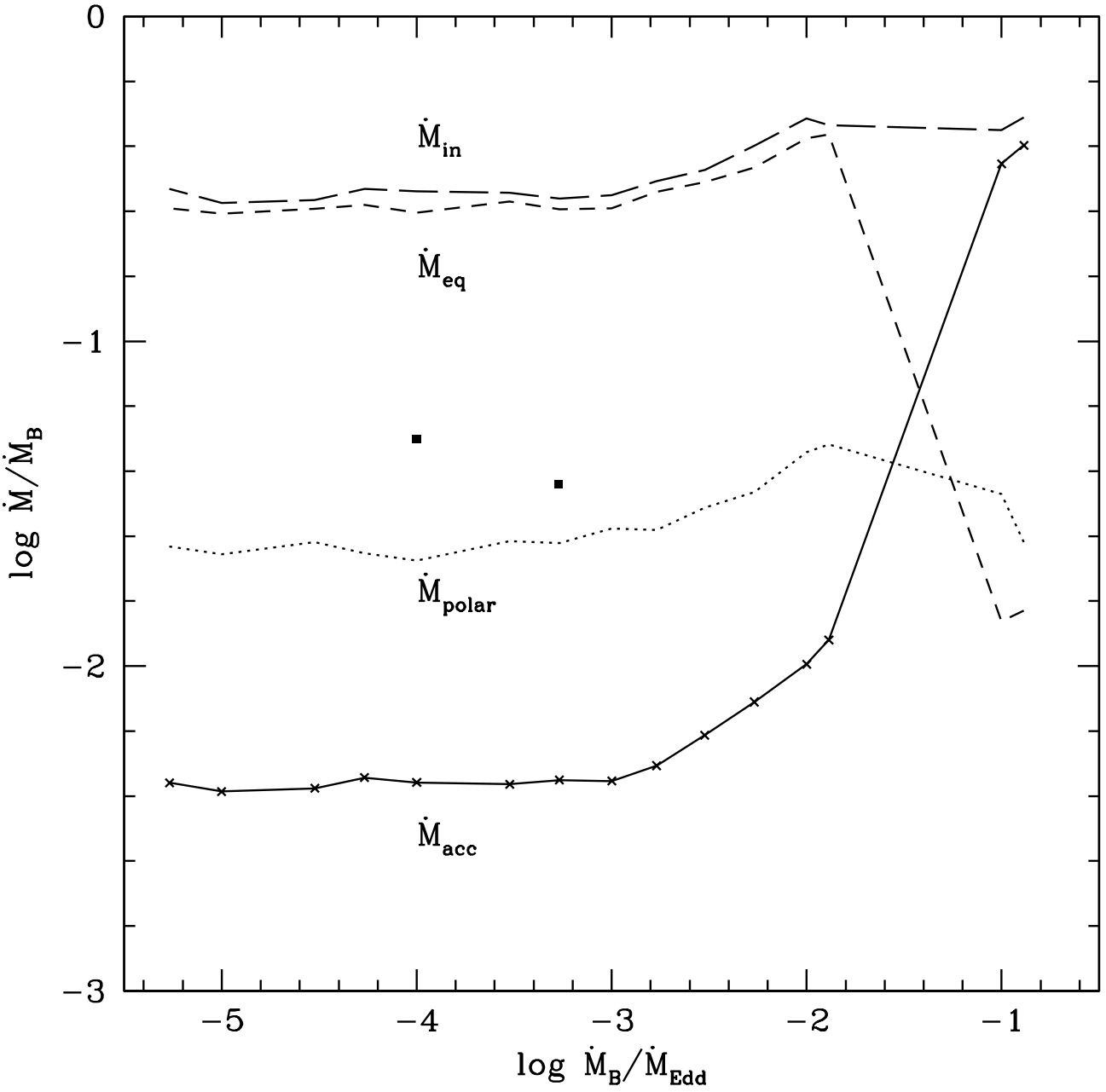

FIG. 6.— Mass inflow rate from large radii, equatorial outflow rate, polar outflow rate (boxes are averages that include episodes of convective overturning), and accretion rate as a function of the Eddington parameter $\dot{M}_{\rm B}/\dot{M}_{\rm Edd}$. At high $\dot{M}_{\rm B}/\dot{M}_{\rm Edd}$ mass inflows at $\sim 1/2$ the Bondi rate and nearly all of it is accreted. At low $\dot{M}_{\rm B}/\dot{M}_{\rm Edd}$, mass again inflows at $\sim 1/2$ Bondi, but nearly all of this matter is deflected outwards in disk outflows. There is an abrupt transition between these distinct solutions in the range $\dot{M}_{\rm B}/\dot{M}_{\rm Edd} \sim 0.01 - 0.1$.

The half-opening angle is typically $\theta_{\rm half-open} \sim 5^\circ$. We show also the half-angles at which half of the mass and half of the momentum in the polar outflows are ejected, again computed at the Bondi radius. The zero density surface in the adiabatic settling solution lies at an angle of $\sim 3^\circ$ at the Bondi radius. Figure 8d shows the mass-flux weighted average wind velocity in the polar outflow, measured at the Bondi radius, as a function of $\dot{M}_{\rm B}/\dot{M}_{\rm Edd}$. The wind velocity can be a significant fraction of the centrifugal velocity

$$v_{\rm c} \equiv (2GM_{\rm BH}/R_{\rm c})^{1/2}, \qquad (17)$$

with typical wind velocity $< v_{\rm wind} > \sim 0.15\, v_{\rm c}$. This value is similar to that found in (Yuan et al. 2012b). The outflow opening angle and velocity depend on the radius at which we measure these quantities. The outflow propagates into a constant density and pressure medium in our setup, and at sufficiently large distances the outflow will transfer its momentum and energy to the ex-

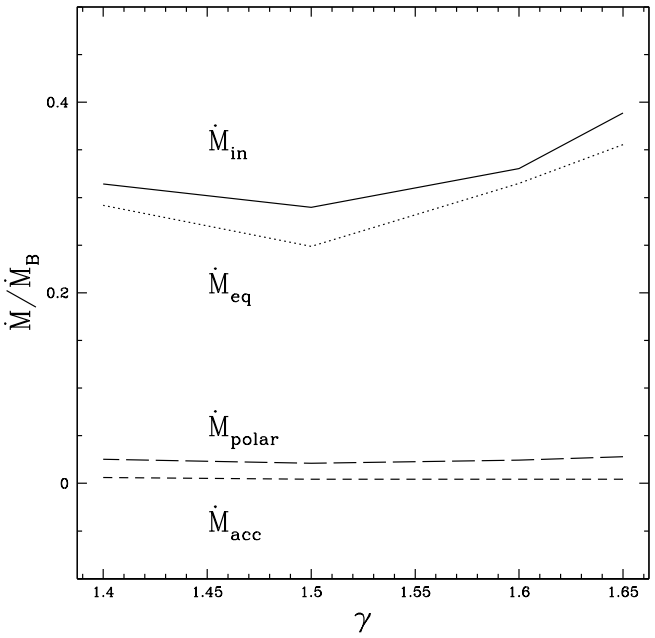

FIG. 7.— Mass inflow rate from large radii, equatorial and polar outflow rates at $R_{\rm B}$, and accretion rate as a function of adiabatic index γ. All solutions are computed for fixed Eddington ratio $\dot{M}_{\rm B}/\dot{M}_{\rm Edd} = 10^{-4}$, the hot disk solutions. Mass fluxes have relatively weak dependence on adiabatic index in the range illustrated, and we set $\gamma = 1.5$ throughout the rest of this work.

ternal medium. Beyond this region the outflow would become subsonic and probably circulate back to join the inflowing gas at intermediate latitudes. We quote values at the Bondi radius to give a quantitative estimate for the outflow properties at a definite radius.

We now discuss in greater detail the radiative properties of our accretion flows. If a spherically symmetric distribution of gas is in free-fall with velocity

$$v_{\rm ff} = (2GM_{\rm BH}/r)^{1/2} \tag{18}$$

and number density

$$n(r) = \frac{\dot{M}_{\rm B}}{4\pi c R_s^2 \eta}(r/R_s)^{-3/2}, \tag{19}$$

where η is the mean mass per electron, then the optical depth

$$\tau \equiv \sigma_T \int n(r) dr \propto \dot{M}_{\rm B}/\dot{M}_{\rm Edd}. \tag{20}$$

We compute the optical depth along three different sightlines with fixed polar angle $\theta = 0°, 45°, 90°$, starting from the inner boundary at $R_{\rm in} = 91R_s$. We find that τ scales linearly with $\dot{M}_{\rm B}/\dot{M}_{\rm Edd}$ (see Figure 8e). The optical depths approach 10^{-2} just below $\dot{M}_{\rm B}/\dot{M}_{\rm Edd} = 10^{-2}$, where the flow switches between the hot, vertically extended disk and the cold, thin disk, and there is a jump by a factor of ~ 100 in τ_{90} at this transition. Further, making use of the temperature profile of an adiabatic gas in free-fall,

$$T \simeq T(R_s)(r/R_s)^{-3(\gamma-1)/2}, \tag{21}$$

the total integrated Bremsstrahlung luminosity

$$L_{\rm Brem}/L_{\rm Edd} \propto \frac{1}{L_{\rm Edd}} \int n(r)^2 T^{1/2} r^2 dr \tag{22}$$

$$\propto (\dot{M}_{\rm B}/\dot{M}_{\rm Edd})^2. \tag{23}$$

Figure 8f shows the Bremsstrahlung luminosity in our simulations integrated over the regions between $R_{\rm in} = 91R_s$ and $0.1R_{\rm B}$, and between $R_{\rm in} = 91R_s$ and the centrifugal torus. We obtain the scaling $L_{\rm Brem}/L_{\rm Edd} \propto (\dot{M}_{\rm B}/\dot{M}_{\rm Edd})^2$ for both integrated luminosities, and $L_{\rm Brem} \to 10^{-7} L_{\rm Edd}$ at $\dot{M}_{\rm B}/\dot{M}_{\rm Edd} = 10^{-2}$. As we move the inner boundary at $R_{\rm in}$ closer to the black hole, we expect the luminosity, temperature, and optical depth interior to the centrifugal radius to increase. Other work including general relativistic and magnetohydrodynamic physics and extending down to the horizon for non-spinning black holes suggests that essentially all matter flowing inwards at our inner boundary $R_{\rm in} = 91R_s$ will ultimately accrete, however (Narayan et al. 2012).

4. DISCUSSION

Observations suggest that the Active Galactic Nuclei (AGN) in nature form a bimodal distribution, with broad-line AGN having accretion rates ~ 2 orders of magnitude higher than narrow-line and lineless AGN (Trump et al. 2009, 2011; Kollmeier et al. 2006; Russell et al. 2012). The transition between these classes occurs at an Eddington ratio between 0.01 and 0.1, in remarkable agreement with our transition between hot and cold flows. Further, the luminosities of the cold and hot disk states suggests a natural feedback loop that can result in switching between the two solutions. From Figure 8 we see that the Bremsstrahlung emission from a cold thin disk can approach $10^{-2} L_{\rm Edd}$ for $\dot{M}_{\rm B}/\dot{M}_{\rm Edd} \sim 0.1$. We do not include the radiative forc-

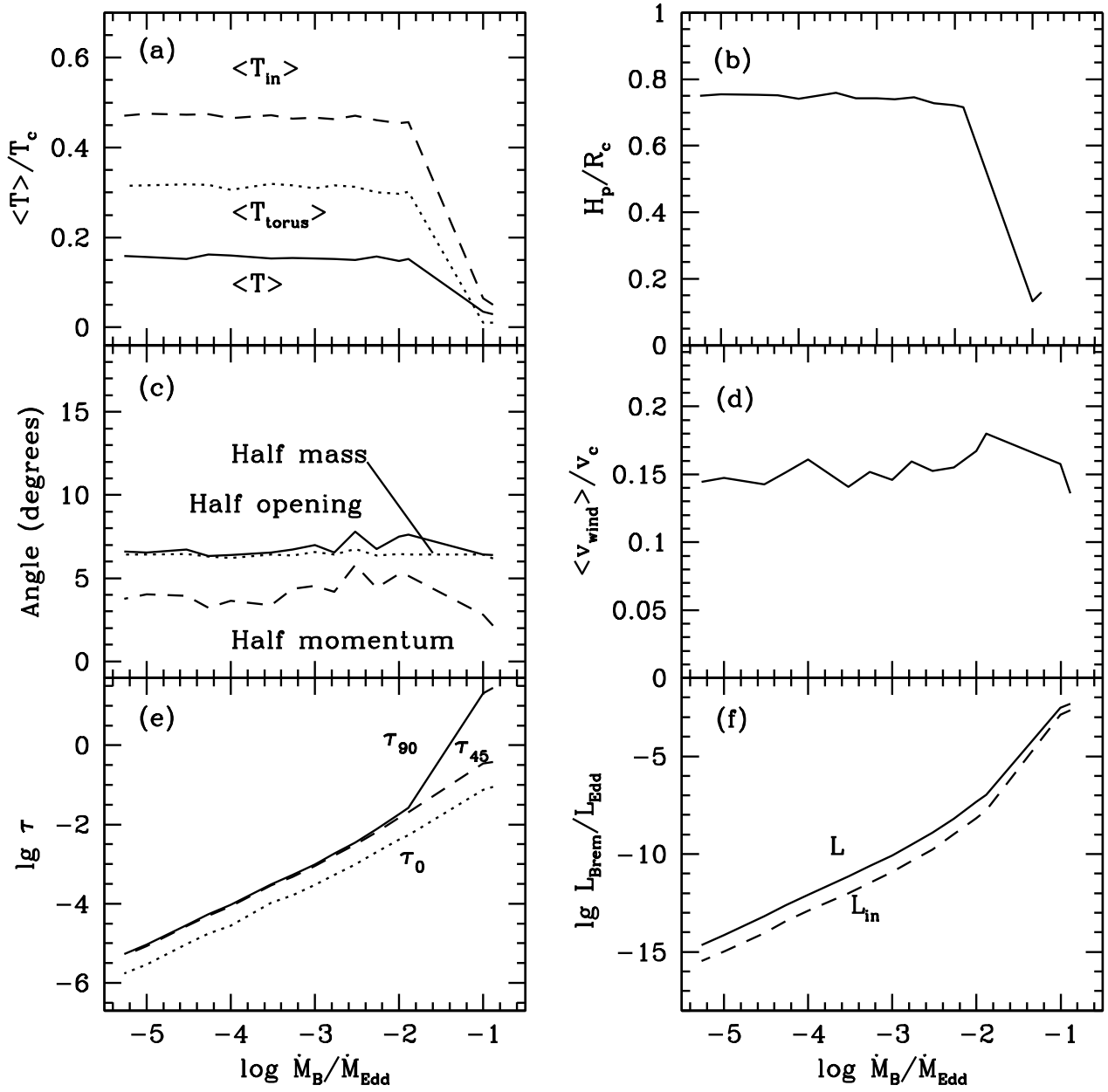

FIG. 8.— 6 characteristic quantities in our solutions, all as a function of $\dot{M}_{\rm B}/\dot{M}_{\rm Edd}$. (a) Emission weighted temperature, averaged over the region interior to the centrifugal torus, the region interior to $0.1R_{\rm B}$, and the centrifugal torus. The low accretion rate solutions are hot, with temperature a sizable fraction of the centrifugal temperature, whereas the high accretion rate solutions are cold. (b) Pressure scale height. The hot disks are vertically extended, with $H_p/R_{\rm c} \sim 0.75$, whereas the cold disks are geometrically thin, with $H_p/R_{\rm c} \ll 1$. (c) Polar wind half-opening angle, measured at $R_{\rm B}$, typically of order 5°. We show also the half-angles at which half the mass and momentum in the wind are ejected. (d) Mass-flux weighted polar wind velocity, measured at $R_{\rm B}$, typically a sizable fraction of the centrifugal velocity. (e) Optical depth along three sightlines with fixed $\theta = 0°, 45°, 90°$. τ scales linearly with $\dot{M}_{\rm B}/\dot{M}_{\rm Edd}$, but there is a jump in τ_{90} when the disk switches to a dense, cold thin disk. The optical depths approach 10^{-2} at $\dot{M}_{\rm B}/\dot{M}_{\rm Edd} = 10^{-2}$. (f) Total Bremsstrahlung luminosity integrated over the region between the inner boundary and $0.1R_{\rm B}$, and between the inner boundary and the centrifugal torus. Luminosity scales as the second power of $\dot{M}_{\rm B}/\dot{M}_{\rm Edd}$ and approaches $10^{-7}L_{\rm Edd}$ at $\dot{M}_{\rm B}/\dot{M}_{\rm Edd} = 10^{-2}$.

ing or thermal heating effects of this emission on infalling gas in our code (Park & Ostriker 2001, 2007; Yuan et al. 2009), but the Bremsstrahlung luminosity would significantly heat the inflowing matter. The disk could transition to the hot, vertically extended state with low accretion, effectively shutting off the Bremsstrahlung emission. In the absence of irradiating photons, the hot disk could then cool and begin accreting at high rates again, thus forming a cycle. This process may be an important detail in explaining the high and low accretion states of quasars (Ciotti & Ostriker 2001). The physics of radiative feedback on supermassive black hole accretion flows has been studied numerically in some detail (Sazonov et al. 2005; Proga 2007; Nagamine et al. 2011; Ciotti et al. 2009, 2010; Kurosawa & Proga 2009; Proga et al. 2008), and a potentially significant effect here would be to increase the strength of the polar outflows.

Independently of any radiative feedback loops, our results indicate that temporal variations in the external boundary conditions at infinity would lead to strongly time-dependent accretion flows. Observations are now approaching sufficient accuracy that for nearby supermassive black holes both the external boundary conditions surrounding the black hole and the reaction of the flow to these external boundary conditions can be measured. Indeed, Gillessen et al. (2012) recently discovered a gas cloud of only several Earth masses orbiting Sgr A* and with radius of closest approach $\sim 3100R_s$. The computations provided here are detailed enough to make concrete predictions concerning the geometrical, dynamical, and thermal properties of accretion disks and outflows of nearby supermassive black holes from currently feasible observations. We do not provide detailed predictions here but may further explore these issues in a separate paper addressing observational consequences.

The lack of magnetic fields is a limitation of our work (Pessah et al. 2008; Beckwith et al. 2009; Penna et al. 2010; Tchekhovskoy et al. 2011; McKinney et al. 2012). Proga & Begelman (2003b) considered the non-radiative two-dimensional magnetohydrodynamic accretion problem, and they find angular momentum transport and accretion driven by the MRI. The two-dimensional structure of the flow determines the accretion properties, with polar outflows quenching the accretion rate. Similar qualitative behavior is present in the Adiabatic Inflow Outflow Solutions (Blandford & Begelman 1999), and we also see circulation and polar outflows in our hydrodynamical simulations with weak cooling. In principle the nonlinear properties of the MRI could modify the detailed structure of the flow in the weak cooling regime. As the cooling rate increases, however, the total energy of the fluid determines its fate and the detailed kinetic properties are less important.

Another extension of our work relates to the enforcement of reflection symmetry through the equatorial plane. The flow does not necessarily need to preserve this symmetry, and in principle there could be asymmetric, unstable modes that seed turbulence and/or convection that modifies the properties of the accretion flow. We have explored this idea in some detail, and we find that the main difference from the presented results to be that the strong equatorial outflow of high angular momentum gas need no longer be centered exactly on the equator, as in Stone et al. (1999) and Yuan et al. (2012a). Asymmetries in bipolar outflows would have clear observational consequences as well, and the behavior of these outflows in different cooling regimes is an avenue of potential research. In any case future studies of the global structure of accretion flows should consider improvements such as fully 3D simulations, general relativistic corrections, self-gravity, and more detailed heat and radiation transport mechanisms. One heat transport mechanism we have studied in some detail at low Eddington ratios is conduction due to thermal electrons (Inogamov & Sunyaev 2010). At lower Prandtl number convective overturning of hot gas can be suppressed, and the strength of the inflow and outflow can vary by a factor of a few. The distribution of outflow between polar and equatorial outflow also depends on the strength of the conduction, but the essential feature of mass accretion rates nearly two orders of magnitude below the Bondi rate remains unchanged.

5. CONCLUSIONS

Our high inflow rate solutions are very similar to the standard and widely adopted Shakura & Sunyaev (1973) results. But our low inflow results are to zeroth order the stationary Papaloizou & Pringle (1984) solution. To next order in the small assumed viscosity they show patterns of circulation, with outflow almost balancing inflow and the net accretion rate through a geometrically thick disk falling to only the order of α (the dimensionless viscous parameter) times the inflow rate. We label this behavior a RRIOS solution for "Radiating, Rotating Inflow-Outflow Solution", as it is a significant generalization of the ADIOS (Adiabatic Inflow-Outflow Solution of Blandford & Begelman (1999)) applicable to the common case wherein the angular momentum load of the inflowing gas strongly restricts the level of net accretion, at low inflow rates. In this low inflow state, viscous forces can drive an equatorial outflow that propagates out beyond the Bondi radius. Further, entropy released by viscous stresses can accumulate near the centrifugal barrier and lead to episodes of convective overturning. Observationally, the solutions that we find appear to be consistent with the fact that most nearby massive black holes show very low bolometric luminosity, considerably below that anticipated for spherically symmetric (non-rotating) Bondi-Hoyle flows, but also show occasional outbursts indicating a much higher rate of episodic outflow.

We thank Jim Stone for many discussions and for help with the ZEUS code. We thank also, Daniel Proga, Feng Yuan, Jim Pringle, Sasha Tchekhovskoy, Yan-Fei Jiang, Bob Penna, Eve Ostriker, Patrick Hall, & Anatoly Spitkovsky for useful comments. The simulations presented in this article were performed on the Orbital and Della clusters supported by the PICSciE-OIT High Performance Computing Center and Visualization Laboratory.

TABLE 1
RESOLUTION DEPENDENCE OF MASS INFLOW RATE AT $R_{\rm B}$, EQUATORIAL AND POLAR OUTFLOW RATES AT $R_{\rm B}$, AND THE ACCRETION RATE FOR $\dot{M}_{\rm B}/\dot{M}_{\rm Edd} = 10^{-4}$.

Resolution	$\dot{M}_{\rm in}/\dot{M}_{\rm B}$	$\dot{M}_{\rm polar}/\dot{M}_{\rm B}$	$\dot{M}_{\rm eq}/\dot{M}_{\rm B}$	$\dot{M}_{\rm acc}/\dot{M}_{\rm B}$
.81	0.32	0.034	0.29	0.0041
1.	0.27	0.021	0.24	0.0042
1.25	0.27	0.020	0.25	0.0044
1.5	0.24	0.020	0.22	0.0045
2	0.21	0.015	0.18	0.0040

TABLE 2
RESOLUTION DEPENDENCE OF MASS INFLOW RATE AT $R_{\rm B}$, EQUATORIAL AND POLAR OUTFLOW RATES AT $R_{\rm B}$, AND THE ACCRETION RATE FOR $\dot{M}_{\rm B}/\dot{M}_{\rm Edd} = 10^{-1}$.

Resolution	$\dot{M}_{\rm in}/\dot{M}_{\rm B}$	$\dot{M}_{\rm polar}/\dot{M}_{\rm B}$	$\dot{M}_{\rm eq}/\dot{M}_{\rm B}$	$\dot{M}_{\rm acc}/\dot{M}_{\rm B}$
.81	0.51	0.061	0.004	0.59
1.	0.45	0.034	0.014	0.35
1.25	0.49	0.033	0.006	0.40
1.5	0.55	0.040	0.001	0.48
2	0.59	0.044	0.001	0.47

APPENDIX

In this Appendix we provide further detail on the general properties of our solutions, including convergence tests. Figure 9 illustrates the time dependence of characteristic quantities in our solutions for Eddington ratio $\dot{M}_{\rm B}/\dot{M}_{\rm Edd} = 10^{-4}$ and computed at our standard resolutions. We show the mass inflow rate at $R_{\rm B}$, equatorial and polar outflow rates at $R_{\rm B}$, and the accretion rate. The mass inflow rate, equatorial outflow rate, and accretion rate are statistically-steady over the illustrated interval. The polar outflow at large radii is punctuated by bursts of convective overturning with high mass outflow rates, but is also quasi-steady after time $t \sim 55 t_{\rm B}$. The simulations of, e.g., Stone et al. (1999) and Yuan et al. (2012a), found persistent convective eddies disrupting mass inflow near the centrifugal support radius, but we find that the thermal energy in the subsonic hot accretion flow with enforced symmetry through the equator can only support intermittent episodes of overturning extending to the Bondi radius. Table 1 shows the dependence of the four quasi-steady mass fluxes from Figure 9 on the spatial resolution of our simulations for the same Eddington ratio $\dot{M}_{\rm B}/\dot{M}_{\rm Edd} = 10^{-4}$. The first column gives the factor by which the number of grid points in each spatial dimension is multiplied. The accretion rate in standard resolution simulation is within 5% of the value at double the grid resolution, and the other mass fluxes are within $\sim 30\%$.

We perform the same exercise at Eddington ratio $\dot{M}_{\rm B}/\dot{M}_{\rm Edd} = 10^{-1}$ and show the quasi-steady average mass fluxes in Table 2. The mass inflow rate at $R_{\rm B}$, polar outflow rate at $R_{\rm B}$, and the accretion rate for the standard resolution simulation are within $\sim 25\%$ of the values in the simulation with double the grid resolution. Note that mass fluxes into and out of our grid do not have to exactly balance during a quasi-steady phase, as there can be a net buildup of gas near the centrifugal radius. This excess gas will eventually be ejected outwards during a convective overturning episode.

We also explored the dependence of our solutions on our choice of no torque inner boundary condition located at $R_{\rm in} = 91 R_s$. We have determined that mass fluxes at large radii change by a factor of 1.1, mass fluxes in the polar region at large radii increase by a factor of 1.2, and accretion rates decrease by a factor of 1.45, as we move the inner boundary to $R_{\rm in} = 91 R_s/2$ for solutions with $\dot{M}_{\rm B}/\dot{M}_{\rm Edd} = 10^{-4}$. Moving the inner boundary inwards by a factor of 4 to $R_{\rm in} = 91 R_s/4$ for the same Eddington ratio reduces the accretion rate by a factor of 2. There is certainly a dependence of accretion flow eigenvalues on the location of the inner boundary (McKinney & Gammie 2002), but the differences do not fundamentally modify the solution types. This scaling of accretion rate with the location of the inner and outer boundaries is also roughly consistent with that found by Yuan et al. (2012a) and Stone et al. (1999). The transition to the cold disks is also pushed to a higher Eddington ratio as the inner boundary is moved inwards. A more self-consistent approach to determining the exact transition Eddington ratio would follow infalling gas down to the black hole horizon.

Anpther variable that can affect the properties of the hydrodynamic accretion flow is the kinematic viscosity. We have explored other values of ν for the hot disk solution at Eddington ratio $\dot{M}_{\rm B}/\dot{M}_{\rm Edd} = 10^{-4}$, and find that the mass inflow rate from large radii is proportional to $\sqrt{\nu}$. The accretion rate as a fraction of the mass inflow rate from large radii appears to scale linearly with the kinematic viscosity.

Finally, in Figure 10 we show the scaling of density with radius for the hot disk solution at $\dot{M}_{\rm B}/\dot{M}_{\rm Edd} = 10^{-4}$. Densities have been averaged over times $t = 55 t_B - 90 t_B$, and the solid curve represents a slice along the equator at $\theta = \pi/2$, whereas the dashed curve represents a slice at constant $\theta = \pi/4$. The equatorial density scales roughly

as $\rho \propto r^{-0.6}$ in the inner parts of the flow interior to the centrifugal support radius at $R_c = 0.02R_B$. Beyond the centrifugal support radius, R_c, the density begins falling more steeply as $\rho \propto r^{-1.2}$, before levelling off in accordance with our outer boundary condition. In comparison, the density scales as $\rho \propto R^{-3/2}$ in ADAF models (Narayan & Yi 1994) and as $\rho \propto R^{-1/2}$ in standard CDAF models (Quataert & Gruzinov 2000; Narayan et al. 2000), though we use a different viscosity prescription.

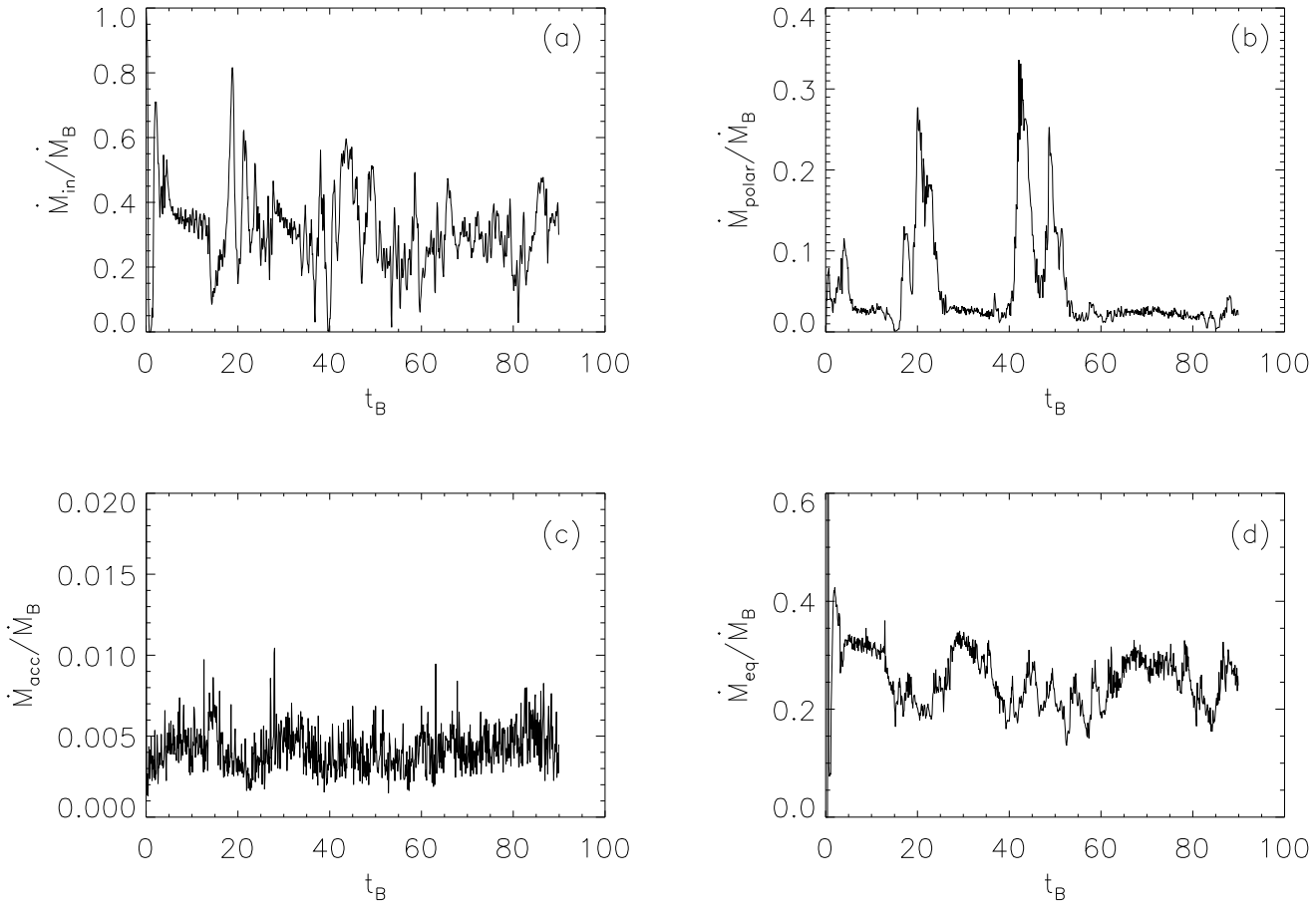

FIG. 9.— Time dependence of mass inflow rate at $R_{\rm B}$, equatorial and polar outflow rates at $R_{\rm B}$, and the accretion rate for the solution at $\dot{M}_{\rm B}/\dot{M}_{\rm Edd} = 10^{-4}$. The simulation has converged to a unique steady-state solution after $t \sim 55t_{\rm B}$.

REFERENCES

Abramowicz, M., Lasota, J. P., & Xu, C. 1986, IAU Symp. 119, 376
Abramowicz, M. A., Czerny, B., Lasota, J. P., & Szuszkiewicz, E. 1988, ApJ, 332, 646
Abramowicz, M., Chen, X., Kato, S., Lasota, J.-P., & Regev, O. 1995, ApJ, 438, L37
Balbus, S. A., & Hawley, J. F. 1991, 376, 214
Ball, G. H., Narayan, R., & Quataert, E. 2001, ApJ, 552, 221
Beckwith, K., Hawley, J. F., & Krolik, J. H. 2009, ApJ, 707, 428
Begelman, M. C., 1978, MNRAS, 243, 610.
Begelman, M. C., & Meier, D. L., 1982, ApJ, 253, 873.
Begelman, M. C. 2012, MNRAS, 2346
Blandford R. D., & Begelman M. C., 1999, MNRAS, 303, L1
Bondi, H. 1952, MNRAS, 112, 195
Chakrabarti, S. K. 1996, ApJ, 464, 664
Chandrasekhar, S. 1960, Proceedings of the National Academy of Science, 46, 253
Chang, K. M., & Ostriker, J. P. 1985, ApJ, 288, 428
Chen, X., & Taam, R. E. 1993, ApJ, 412, 254
Ciotti, L., & Ostriker, J. P. 2001, ApJ, 551, 131
Ciotti, L., Ostriker, J. P., & Proga, D. 2009, ApJ, 699, 89
Ciotti, L., Ostriker, J. P., & Proga, D. 2010, ApJ, 717, 708
Dibi, S., Drappeau, S., Fragile, P. C., Markoff, S., Dexter, J. 2012, arXiv:1206.3976
Eggum, G. E., Coroniti, F. V., & Katz, J. I., 1988, ApJ, 330, 142.
Fishbone, L. G., & Moncrief, V. 1976, ApJ, 207, 962
Fragile, P. C., Gillespie, A., Monahan, T., Rodriguez, M., Anninos, P. 2012, ApJS, 201, 9
Frank, J., King, A., & Raine, D. 2002, Accretion Power in Astrophysics (Cambridge: Cambridge University Press)
Gillessen, S., Genzel, R., Fritz, T. K., et al. 2012, Nature, 481, 51
Hawley J. F., Balbus S. A., & Stone J. M., 2001, ApJ, 554, L49
Hawley J. F., & Balbus S. A., 2002, ApJ, 573, 738
Hawley, J. F., Guan, X., & Krolik, J. H. 2011, ApJ, 738, 84
Hawley J. F., & Smarr, L. L. 1986, AIPC, 144, 263
Hawley J. F., Smarr, L. L., & Wilson, J. R. 1984a, ApJ, 277, 296
Hawley J. F., Smarr, L. L., & Wilson, J. R. 1984b, ApJS, 55, 211
Ichimaru, S., 1977, ApJ, 214, 840.
Igumenshchev, I. V., 2006, ApJ, 649, 361
Igumenshchev I. V., & Narayan R., 2002, ApJ, 566, 137

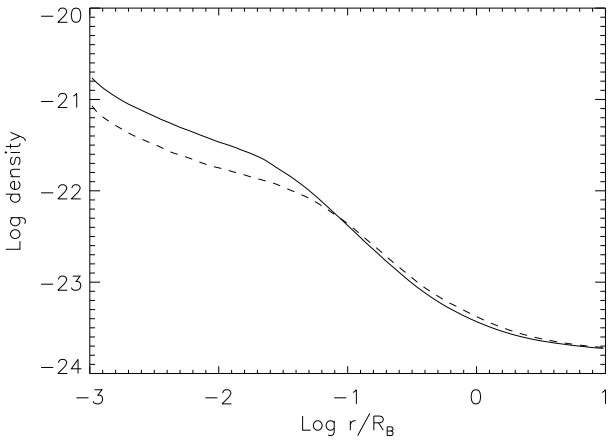

FIG. 10.— Scaling of density with radius for the hot disk solution at $\dot{M}_{\rm B}/\dot{M}_{\rm Edd} = 10^{-4}$. The solid curve corresponds to a slice along the equator, and the dashed curve corresponds to a slice at $\theta = \pi/4$.

Igumenshchev I. V., & Abramowicz M. A., 1999, MNRAS, 303, 309
Igumenshchev I. V., & Abramowicz M. A., 2000, ApJS, 130, 463
Igumenshchev I. V., Abramowicz M. A., & Narayan, R., 2000, ApJ, 537, 27
Igumenshchev I. V., Narayan, R., & Abramowicz M. A., 2003, ApJ, 592, 1042
Inogamov N. A., & Sunyaev R. A., 2010, Astron. Lett., 36, 835
King, A. R., Pringle, J. E., & Livio, M. 2007, MNRAS, 376, 1740
Janiuk, A., Sznajder, M., Moscibrodzka, M., & Proga, D. 2009, ApJ, 705, 1503
Jiao, C. L., & Wu, X. B. 2011, ApJ, 733, 112
Kato, S., Honma, F., & Matsumoto, R. 1988, MNRAS, 231, 37
Katz, J., 1977, ApJ, 215, 265.
Kollmeier, J. A. et al. 2006, ApJ, 648, 128
Kolykhalov, P. I.,& Syunyaev, R. A. 1979, SvAL, 5, 180
Kolykhalov, P. I.,& Syunyaev, R. A. 1980, SvAL, 6, 357
Kurosawa, R., Proga, D., & Nagamine, K. 2009, ApJ, 707, 823
Lynden-Bell, D., & Pringle, J. E., 1974, MNRAS, 168, 603.
Machida, M., Matsumoto, R., & Mineshige, S. 2001, PASJ, 53, 1
McKinney, J. C., & Gammie, C. F. 2002, ApJ, 573, 728
McKinney, J. C., Tchekhovskoy, A., & Blandford, R. D. 2012, MNRAS, 423, 3083
Moscibrodzka, M., & Proga D. 2003, ApJ, 679, 626
Moscibrodzka, M., & Proga D. 2009, MNRAS, 397, 2087
Nagamine, K., Barai, P., & Proga, D. 2011, arXiv1112.3525
Narayan, R., Igumenshchev, I. V., & Abramowicz, M. A. 2000 ApJ, 539, 798
Narayan, R., & Popham, R. 1993, Nature, 362, 820
Narayan, R., & Yi, I. 1994, ApJ, 428, L13
Narayan, R., & Yi, I. 1995a, ApJ, 452, 710
Narayan R., & Yi I., 1995b, ApJ, 452, 710
Narayan, R., & Fabian, A. C. 2011, MNRAS, 415, 3721
Narayan, R., & McClintock, J. E. 2008, NewAR, 51, 733
Narayan, R., Sadowski, A., Penna, R. F., & Kulkarni, A. K. 2012, arXiv1206.1213
Novikov, I. D., & Thorne, K. S. 1973, in Blackholes ed. C. DeWitt & B. DeWitt, 343, Gordon & Breach.
Ohsuga, K., Mineshige, S., Mori, M., Kato, Y., 2009, PASJ, 61, 7
Ohsuga, K., & Mineshige, S., 2011, ApJ, 736, 2
Papaloizou, J. C. B., & Pringle, J. E., 1984, MNRAS, 208, 721
Papaloizou, J. C. B., & Pringle, J. E., 1987, MNRAS, 225, 267
Park, M. G. 2009, ApJ, 706, 637
Park, M. G., & Ostriker, J. P. 2001, ApJ, 549, 100
Park, M. G., & Ostriker, J. P. 2007, ApJ, 655, 88
Pang, B., Pen, U. L., Matzner, C. D., Green, S. R., Liebendörfer, M. 2011, MNRAS, 415, 1228
Pen, U. L., Matzner, C. D., Wong, S. 2003, ApJ, 596, 207
Penna, R. F., McKinney, J. C., Narayan, R., et al. 2010, MNRAS, 408, 752
Pessah, M. E., Chan, C.-K., & Psaltis, D. 2008, MNRAS, 383, 683
Pringle J. E., 1981, ARA&A, 19, 137
Proga, D. 2007, ApJ, 661, 693
Proga D., & Begelman M. C., 2003a, ApJ, 582, 69
Proga D., & Begelman M. C., 2003b, ApJ, 592, 767
Proga, D., Ostriker, J. P., & Kurosawa, R. 2008, ApJ, 676, 101
Quataert, E. 2004, ApJ, 613, 322
Quataert, E., & Narayan, R. 1999a, 1999, ApJ, 516, 399
Quataert, E., & Narayan, R. 1999b, ApJ, 520, 298
Quataert, E., & Narayan, R. 2000, ApJ, 528, 236
Quataert E., & Gruzinov A., 2000, ApJ, 539, 809
Rees, M. J., Begelman, M. C., Blandford, R. D., & Phinney, E. S. 1982, Nature, 295, 17.
Russell, H. R., McNamara, B. R., Edge, A. C., et al. 2012, arXiv:1211.5604
Sazonov, S. Y., Ostriker, J. P., Ciotti, L., & Sunyaev, R. A. 2005, MNRAS, 358, 168
Shakura, N. I., & Sunyaev, R. A. 1973, A&A, 24, 337
Sharma, P., Quataert, E., & Stone, J. M. 2008, MNRAS, 389, 1815
Shcherbakov, R. V. 2010, ApJ, 716, 504
Stone, J. M., & Norman, M. L. 1992, ApJS, 80, 753
Stone, J. M, Hawley, J. F., Gammie, C. F. & Balbus, S. A. 1996, ApJ, 463, 656
Stone, J. M., Pringle, J. E., & Begelman, M. C. 1999, MNRAS, 310, 1002
Stone J. M., & Pringle J. E., 2001, MNRAS, 322, 461
Svensson, R. 1982, ApJ, 258, 335
Tchekhovskoy, A., Narayan, R., & McKinney, J. C. 2011, MNRAS, 418, L79
Trump, J. R. et al. 2009, ApJ, 700, 49
Trump, J. R. et al. 2011, ApJ, 733, 60
Velikhov, E. P. 1959, Soviet Phys. JETP Lett., 36, 995.
Wilson, J. R. 1972, ApJ, 173, 431
Xu, G., & Chen, X. 1997, ApJ, 489, 29
Yuan, F., Peng, Q., Lu, J. F., & Wang, J. 2000, ApJ, 537, 236
Yuan, F., Bu, D., 2010, MNRAS, 408, 1051
Yuan F., Bu D., Wu M., 2012, arXiv:1206.4173
Yuan, F., Quataert, E., & Narayan, R., ApJ, 2003, 598, 301
Yuan F., Wu M., Bu D., 2012, arXiv:1206.4157
Yuan, F., Xie, F., Ostriker, J. P., ApJ, 2009, 691, 98
Zanotti, O., Roedig, C., Rezzolla, L., & Del Zanna, L. 2011, MNRAS, 417, 2899